ADVANCED FUNCTIONAL MATERIALS
www.afm-journal.de

Magnesium Test: Universal and Ultra-Sensitive Method for Measuring Reliability of Thin-Film-Encapsulated Bioelectronic Implants in Physiological Environment

Massimo Mariello, Kosuke Ayama, Kangling Wu, Costanza Baudino, Lei Wang, Léo Mutschler, Lucas Aurélien Jourdan, Marion Bianca Cleusix, Ivan Furfaro, Claudia Kathe, Grégoire Courtine, Marion von Allmen, Matthias Van Gompel, Yves Leterrier,* and Stéphanie P. Lacour**

Next-generation bioelectronic implants require miniaturization, durability, and long-term functionality. Thin film encapsulations, prepared with inorganic or hybrid organic/inorganic designs, are essential for ensuring protection, low water permeation, adaptability, and structural strength. It is equally important to precisely measure their barrier performance, especially for in vivo use, to ensure the manufacture of reliable bioelectronics. Current monitoring solutions are not adequate: they are bulky, lack sensitivity, and are incompatible with microfabricated devices. Here, a comprehensive method is introduced to quantify the permeability of thin-film encapsulation for bioelectronic implants both in situ and in real time. This method relies on monitoring the electrical resistance of the Mg film, which experiences corrosion due to water permeation, leading to Mg hydrolysis. An analytical model is proposed that predicts and quantifies this permeation, and is adaptable for various types of encapsulations, including hybrid multilayers. An unprecedented ultra-low detection limit of 3×10^{-8} g m^{-2} d^{-1} at room temperature is demonstrated and the monitoring approach is validated in vivo using polyimide and poly(dimethylsiloxane)-coated bioelectronics.

1. Introduction

The next-generation implantable bioelectronic devices will be microfabricated, soft, and compliant to the host tissues. Compelling demonstrations of these devices have been deployed in animal models (rodents[1] minipigs,[2] non-human primates[3]) and humans,[4] with a particular application focus on medical technologies. To operate over years in vivo and guarantee their form factor, they should be protected from the body environment by thin, high-barrier coatings, called hereafter thin film encapsulation (TFE), whose design, synthesis, and integration represent a critical challenge. The main function of the TFE is to guarantee simultaneous compatibility with microfabrication processes, mechanical compliance, biocompatibility, hermeticity, and long-term reliability.[5–8] Against standard barrier

M. Mariello[+], K. Wu, I. Furfaro, S. P. Lacour
École Polytechnique Fédérale de Lausanne
School of Engineering
Neuro-X Institute
Geneva CH-1202, Switzerland
E-mail: massimo.mariello@eng.ox.ac.uk; stephanie.lacour@epfl.ch
M. Mariello[+], Y. Leterrier
Laboratory for Processing of Advanced Composites (LPAC)
École Polytechnique Fédérale de Lausanne (EPFL)
Lausanne CH-1005, Switzerland
E-mail: yves.leterrier@epfl.ch

The ORCID identification number(s) for the author(s) of this article can be found under https://doi.org/10.1002/adfm.202315420

[+]Present address: Institute of Biomedical Engineering (IBME), Department of Engineering Science, University of Oxford, Oxford OX3 7DQ, UK

DOI: 10.1002/adfm.202315420

K. Ayama, C. Baudino, L. Wang, L. Mutschler, L. A. Jourdan, M. B. Cleusix
École Polytechnique Fédérale de Lausanne (EPFL)
Lausanne CH-1005, Switzerland

C. Kathe, G. Courtine
École Polytechnique Fédérale de Lausanne
School of Life Sciences
Neuro-X Institute
Geneva CH-1202, Switzerland

C. Kathe, G. Courtine
Defitech Center for Interventional Neurotherapies (NeuroRestore)
University Hospital Lausanne (CHUV)
University of Lausanne and EPFL
Lausanne CH-1011, Switzerland

G. Courtine
Department of Clinical Neurosciences
Lausanne University Hospital (CHUV) and University of Lausanne (UNIL)
Lausanne CH-1011, Switzerland

G. Courtine
Department of Neurosurgery
CHUV
Lausanne CH-1011, Switzerland

technologies (based on macroscopic rigid Titanium or ceramic capsules, or on thick silicones[9]), current TFE exploit organics (e.g., polyimide,[10] Teflon,[11] parylene C[12]), inorganics (e.g., aluminum oxide (Al_2O_3), silicon dioxide (SiO_2, SiO_x),[13] silicon nitride (SiN_x),[14] silicon carbide (SiC)[13,14]), or a combination of the two, deposited by atomic layer deposition (ALD), chemical vapor deposition (CVD) or thermal growth.[15–19] Table S1 (Supporting Information) compiles the best-known materials for flexible/stretchable encapsulations, while for a recent review on TFE, please refer to ref. [5]. While there are no universally defined metrics to quantify the performance of TFE, one can report the Water Vapor Transmission Rate (WVTR).[5] This metric indicates how much moisture can penetrate through the TFE over a specific period. Throughout the paper, we use WVTR for referring to exposure to wet air (water vapor), and WTR (Water Transmission Rate) for exposure to liquid water. Another useful parameter, especially for TFEs prepared with inorganic films, is the Crack Onset Strain (COS), which informs about the maximum strain before the film experiences catastrophic cracking.[20–22] Ideally TFE for bioelectronic implants should offer ultra-low WTR ($<10^{-4}$ g m^{-2} d^{-1}), high COS, and designs complying with tissue anatomy and biomechanics to guarantee a functional lifetime of at least 5–10 years in the body.[21,23–27] Recent strategies include multilayer architectures, consisting of alternating dyads made of organic and inorganic layers.[7,28,29] However, one of the main challenges for the implementation of these TFEs is the accurate evaluation of their barrier properties, because standard measuring systems usually display high detection limits ($>10^{-5}$ g m^{-2} d^{-1}). Recent and accurate methods (e.g., the calcium (Ca) test[5,30–33]) are not fully compatible with miniaturization/microfabrication processes, thus not suitable for flexible bioelectronics form factors.

In this study, we propose a comprehensive, robust, and in situ method to quantify ultra-low permeability of TFE engineered for bioelectronic micro-devices.[6] The method relies on Mg thin-film electrical sensors, called "e-Mg test cards". The fundamental principle is that corrosion of Mg into $Mg(OH)_2$, caused by water diffusion through the barrier coating is continuously monitored by analyzing via the electrical resistance of the Mg structures. Differently from Ca, which reacts vigorously (<10 s) with oxygen and water,[34] Mg films can be deposited and processed in a standard atmosphere and easily integrated into the microfabrication processes of bioelectronic implants. We demonstrate that the method is universal as it can be applied to various types of TFE barrier encapsulation and testing conditions, from wet air to in vivo environments. The method is complementary to the Mg optical permeability test that we recently proposed to quantify water-side permeation in thin-film encapsulations.[35]

We deployed TFE-coated Mg test cards in rigid, flexible, and stretchable formats and assessed the impact of mechanical deformation of the TFE on water permeation. Finally, we implemented the in-situ Mg test sensors into two representative bioelectronic implants interfacing the surface of the brain (**Figure 1**) and the spinal cord.

M. von Allmen, M. Van Gompel
Comelec SA
La-Chaux-de-Fonds 2300, Switzerland

2. Results

2.1. Corrosion of Magnesium Thin Films

2.1.1. Magnesium Corrosion without Encapsulation Layers

Mg films (200 nm thick) are deposited and patterned on rigid electrical Mg (e-Mg) test cards (Figure S1, Supporting Information), i.e., glass carrier pre-patterned with inert metallic (Ti/Pt/Au) tracks (Figure S2a, Supporting Information). The full fabrication process is reported and described in Note S2 and Figure S3 (Supporting Information).

Each Mg pattern is soldered to customized flexible printed circuit boards (PCBs) or flexible cables (Figure S2b–e, Supporting Information) with connections supporting a 4-point probe (4PP) monitoring of the Mg resistance (Figure S2f, Supporting Information). Wire soldering adds negligible resistance to that of the Mg pattern. All contacts are sealed using poly(isobutylene) or PIB.[36,37] See the details in Note S6 (Supporting Information).

The Mg patterns eventually become transparent regardless of the water-based environment, but how it gets to this state can vary (**Figure 2a**; Figure S5a, Supporting Information). In PBS, which contains ions like chloride (Cl^-) or sodium (Na^+), the Mg turns brown on the surface. This color change is due to the formation of corrosion by-products (Figure S5b, Supporting Information).

Next, we monitored how thick the Mg patterns became in different environments: DI H_2O, saline solution, and hot and wet air (Figures S6–S8, Supporting Information; Figure 2b). In the first two cases, the Mg first thickens and then thins out until it disappears. This happens because the Mg reacts with water to form hydroxide, which then dissolves into the water ($Mg + 2H_2O \rightarrow Mg(OH)_2 + H_2$; Figure 2c). In humid air, however, the Mg thickens and then stabilizes, indicating that the corrosion products stay in place leading to five times increase in the thickness. This trend is consistent regardless of the initial thickness of the Mg (from 20 nm to 1 µm; Figure S9, Supporting Information). This can be ascribed to the adsorption of water molecules that solvate the Mg ions yielding a loose hydroxide structure with lower mass density than that of the bulk material.[38]

The transformation into hydroxide is confirmed by X-ray diffraction (XRD), with clear peaks for Mg and $Mg(OH)_2$. During the corrosion process, the (002) peak at 34.38° decreases in intensity while the (001) peak at 18.75° increases.[39,40] Both peaks are the strongest and indicate hexagonal structures. This suggests that while oxidation alters the mass density, it does not change the crystal structure.[41] In terms of surface morphology, corrosion manifests non-uniformly, initially presenting as black spots and porous islands termed pinhead defects. These can be observed in the optical (Figure 2d), SEM (Figure 2e), and AFM (Figure 2f) micrographs. When exposed to wet air (Figure S10a, Supporting Information), this inhomogeneity exacerbates with the Mg roughness, sometimes to the extent of hundreds of nm or even µm. Additionally, the density of the hydroxide pinhead-like defects on the surface increases with longer exposure time (Figure S10b, Supporting Information). When in direct contact with liquid (PBS), Mg corrodes faster and more aggressively, leading to an unpredictable and irregular surface morphology (Figure S10c, Supporting Information).

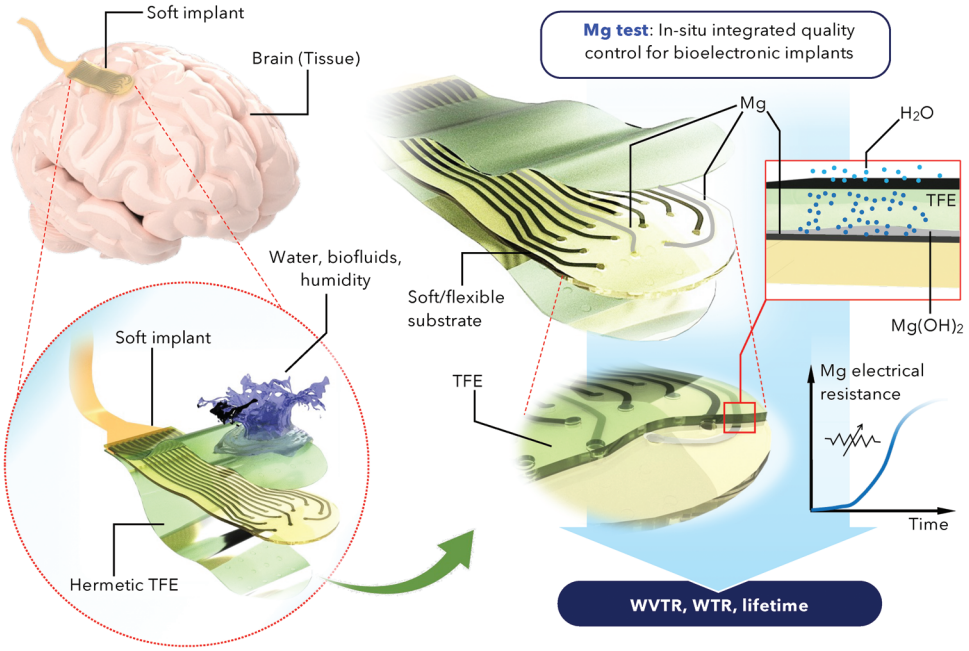

Figure 1. Concept of Magnesium test. Schematic showing a compliant electrode implant (electrocorticography array) deployed on the surface of the cortex. The implant needs hermetic thin-film encapsulations (TFE) for chronic applications, in order to be protected against water, biofluids, and humidity ingress. Mg test is introduced as an accurate in situ method for barrier assessment. Mg corrosion and conversion into hydroxide ($Mg(OH_2)$) is harnessed to quantify the encapsulation's transmission rate.

As corrosion progresses, the initially conductive Mg film becomes thinner as it converts to hydroxide, resulting in a steady rise in electrical resistance (R_{Mg}) up to an equivalent open circuit (infinite resistance). The corrosion rate accelerates with increasing exposure temperatures, aligning with the principle of thermally activated electrochemical reactions. This is nicely illustrated in Figure 2g with R_{Mg} monitored in water vapor at 85%RH and over three different aging temperatures (37, 67, and 85 °C; Figure S12a,b, Supporting Information). The variation rate of R_{Mg}, can be correlated with the WVTR of a barrier coating. The WVTR derived from the resistance measurement ($WVTR_{meas}$) is calculated as follows:

$$WVTR_{meas} = K \cdot \frac{1}{R_{Mg}^2}\frac{dR_{Mg}}{dt} \quad (1)$$

where $K = -n(M_{H_2O}/M_{Mg})(S_{Mg}/S)(l/w)\delta\rho$ is a constant depending only on geometrical and physical parameters of the Mg pattern under corrosion; $n = 2$ is the number of equivalent electrons transferred in the corrosion reaction; $M_{Mg} = 24\ g\ mol^{-1}$ and $M_{H_2O} = 18\ g\ mol^{-1}$ are the molar masses of Mg and water, respectively; S_{Mg}, *and* S are the surface areas of Mg directly exposed to corrosion and of the barrier permeated by water, respectively; l, w are the effective length and width of the Mg pattern; δ, ρ are the Mg mass density (1.738 g cm^{-3},[42]) and electrical resistivity (1.63×10^{-6} Ω m, at 25 °C[43]), respectively. Equation (1) can be adopted both for WVTR and WTR.

It should be noted that there is not an established correlation between WVTR and WTR, since a relative humidity of 100% does not correspond to a liquid environment.[44] The analytical model (see the full derivation in the Supporting Information) is based on the assumption of a homogeneous variation of the Mg thickness profile, as it was observed experimentally (Figures S6–S8, Supporting Information), i.e., a gradual decrease of the metal thickness, in favor of an increasing thickness of hydroxide layer (see the empirical models illustrated in Figure S13a,b, Supporting Information). Therefore, since the hydroxide acts as an additional inorganic barrier, which hinders and delays the corrosion of Mg underneath, the corrosion rate of Mg can be correlated with the WVTR of the $Mg(OH)_2$ layer, through Equation (1). In Figure 2h, the WVTR curves show a decreasing trend due to the increasing thickness of the hydroxide layer (see Figure 2b), indicating a constant hydroxide permeability[45]). The averaged WVTR values measured before conductivity loss are 1.1×10^0, 4.0×10^{-1}, 8.2×10^{-3} g m^{-2} d^{-1} for 85, 67, and 37 °C, respectively, all at 85% RH. An activation energy of 4.32 kcal mol^{-1} (18 kJ mol^{-1}) was obtained for water permeation into $Mg(OH)_2$ (see Equation S21 in the Supporting Information and illustrated in the Arrhenius plot in Figure 2i). This value is lower than those reported for glassy or crystalline oxides,[46] likely due to the high porosity of the Mg hydroxide.

2.1.2. Magnesium Corrosion with Encapsulation Layers

Next, we characterized e-Mg test cards coated with standard TFE. We selected parylene C which is deposited by CVD at room temperature[47] and is very commonly used as a packaging conformal layer for electronic circuits.[17,48] The resistance curves and WVTR data for parylene-coated test cards exposed to wet air (85 °C, 85%RH) with two different parylene thicknesses (2 µm and 5 µm) are presented in **Figure** 3a,b, respectively, with detailed

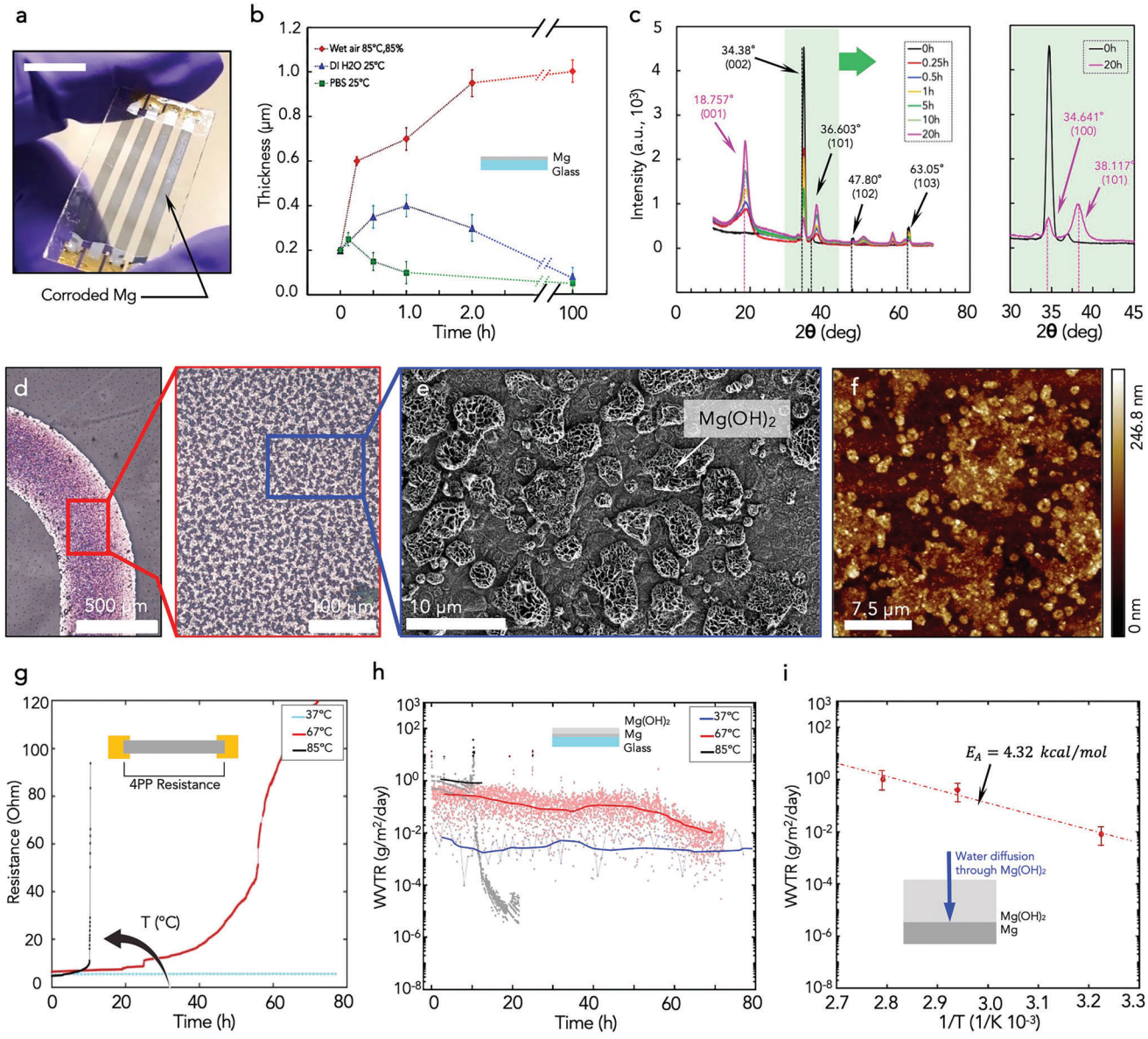

Figure 2. Corrosion of Mg thin films without encapsulations. a) Corroded Mg test card with the ends protected by the PIB sealant. Scale bar: 1 cm. (b) Summary plot for the thickness profiles over time for different testing conditions: wet air 85 °C, 85%RH, PBS 25 °C, de-ionized water 25 °C. c) XRD spectra of corroding Mg thin films (≈200 nm), with an indication of the main characteristic peaks. d) Corroded Mg track (in wet air 85 °C, 85%RH) with optical micrograph showing black corrosion spots. e) SEM image of the corroded Mg surface with the presence of porous islands. f) AFM topography image of the corroded Mg surface. g–i) Electrical monitoring of the corroding rigid test cards at three different temperatures and fixed 85% relative humidity: g) resistance versus time curves, h) WVTR of the $Mg(OH)_2$ film (calculated with Equation (1)) versus time datapoints and smoothed averaged curves, The "noise" is due to intrinsic signal fluctuations by the electronic instrumentation. i) Arrhenius plot.

point-to-point descriptive analysis in Figure S14 (Supporting Information). A similar signature is evident for the two investigated thicknesses and reflects the intricate diffusion and corrosion phenomena at work. It is also evident that the thicker barrier delays the Mg corrosion as revealed from the final asymptotes in both resistance and WVTR data. Time "0" corresponds to the start of data recording, when the samples are introduced in the environment at the set conditions. The difference between the initial resistances for the two parylene thicknesses is attributed to minor differences in fabrication patterning, electrical connections, and overlap between Mg and Au. The temperature at the parylene/Mg interface reaches 85 °C within less than 1 ms, based on a heat equation approximation, so that one can ignore transient thermal effects. The lag time for the diffusion of water molecules from the outer surface to the parylene/Mg interface was also evaluated using Fick's second law and an estimated diffusion coefficient at 85 °C. It was found to be close to 1 s and 6 s the for 2 and 5 μm parylene layers, respectively, which means that the corrosion process of Mg starts almost immediately at the experimental timescale.

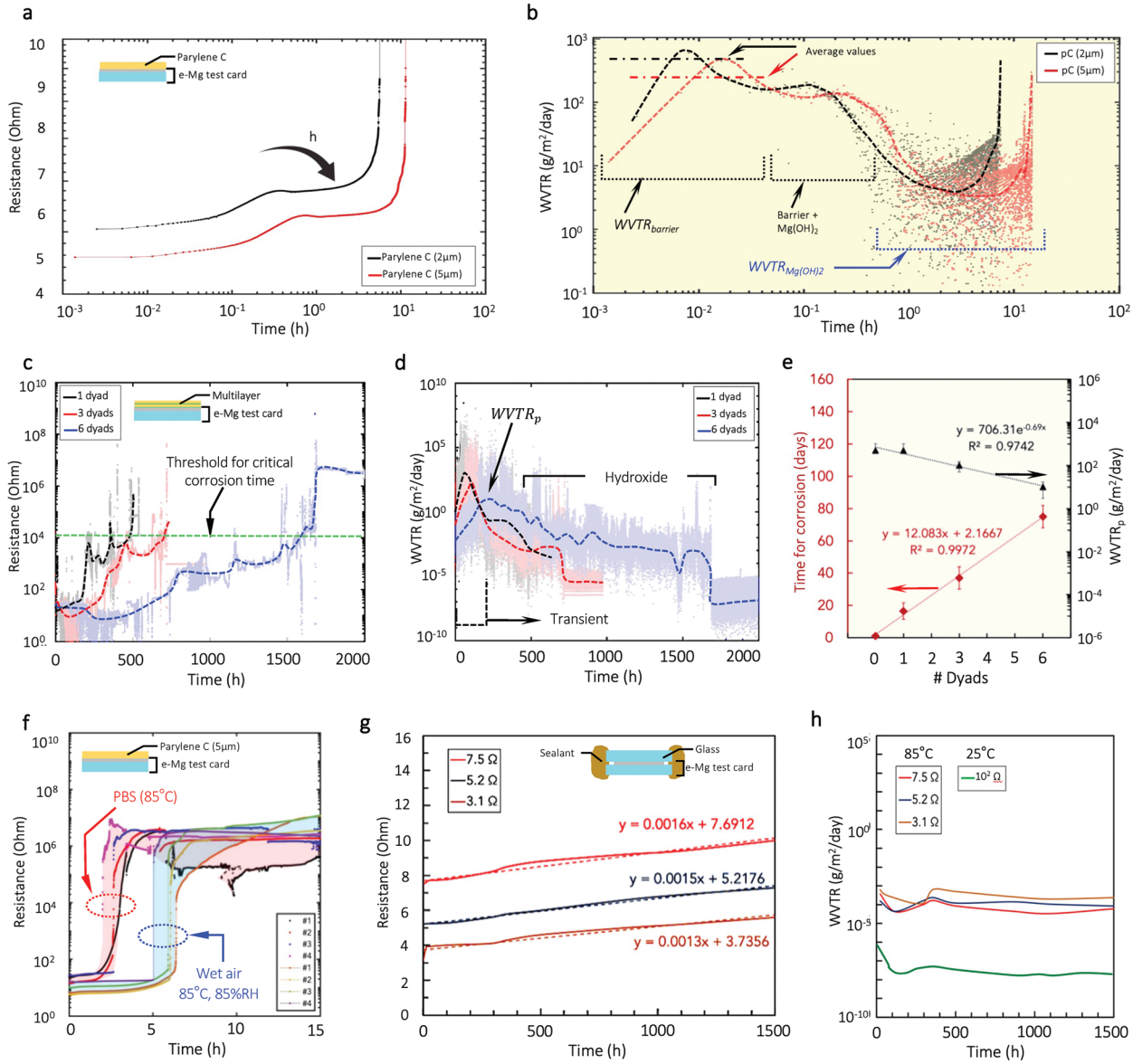

Figure 3. Reproducibility, sensitivity, and validation of e-Mg test. a,b) Electrical monitoring of the corroding rigid test cards coated with parylene C with two thicknesses (2 µm and 5 µm), at 85 °C and 85% relative humidity: a) resistance curves, b) WVTR curves. The inset in (a) shows the initial range of the resistance curves, below 10Ω. The inset in (b) shows the different ranges of the WVTR curves, highlighting the final formation of Mg hydroxide. c,d) Electrical monitoring of the corroding rigid test cards coated with multilayer hybrid encapsulations (1, 3, 6 dyads), at 85 °C and 85% relative humidity: c) resistance curves, d) WVTR curves (e) plot of time for corrosion and of WVTR (peak) versus number of dyads. f) Resistance and WVTR curves for four samples coated with parylene C, for testing reproducibility in wet air and in liquid. g,h) Measurements for determining the low detection limit: (g) resistance monitoring, (h) WVTR curves.

In a first, initial regime the resistance progressively increases until it reaches a plateau value after several 10 min, a result of the initial corrosion steps. During this first phase, the WVTR starts to increase because more and more molecules permeate the barrier per unit time and it goes through a maximum after few 10 s. At this point, the concentration of water molecules at the interface and the Mg corrosion rate are maximum. The measured WVTR (Equation 1) results from the combined influence of the barrier and the forming hydroxide. The WVTR of the barrier (WVTR) was then deduced by adopting the theory of permeability in laminates/multilayers (Figure S13c, Supporting Information), as follows (see also Equation S45 in the Supporting Information), using the known WVTR of the hydroxide (Figure 2):

$$WVTR = \left(\frac{1}{WVTR_{meas}} - \frac{1}{WVTR_{Mg(OH)_2}} \right)^{-1} \quad (2)$$

The datapoints derived from Equation (2) represent the effective WVTR of the barrier, taking into account also the initial non-homogeneous formation of the discontinuous hydroxide layer. At 85 °C, 85%RH parylene C exhibited an average WVTR of (5.1 ± 0.5) × 10^2 and (2.0 ± 0.3) × 10^2 g m^{-2} d^{-1} for 2 and 5 µm

thicknesses, respectively, in accordance with values reported in literature.[49] These values are determined as an integral mean of the WVTR curve in the initial regime of the measurement: a detailed description of how they are calculated is reported in the next section.

The decrease of WVTR which follows is due to the progressive formation of the porous hydroxide layer, acting as an additional barrier for the diffusion of water molecules. The second regime in the resistance behavior starts with a plateau until a final massive increase. This change in the resistance increase is essentially due to a slow-down of the corrosion and reduction of the Mg thickness due to the presence of a growing hydroxide barrier. The critical time for full corrosion is reached asymptotically when the Mg thickness goes to zero, and the resistance diverges up to MΩ due to the loss of electrical connection. The WVTR in this second regime decreases because the thickness of the hydroxide increases (here the scatter is higher in the logarithmic representation, also due to a higher variability in the discretely computed temporal derivative of the Mg resistance).

Next, we prepared test cards with high-barrier encapsulations consisting of multilayer hybrid sequences of organic and inorganic thin films[7] (Figure S15a, Supporting Information). In particular, we designed a multilayer structure made of repeated dyads of 500 nm-thick parylene C and an ALD Al_2O_3 (30 nm)/TiO_2 (5 nm) inorganic bilayer.[7,50] The barriers were grown and deposited at low temperature (<100 °C) in a hybrid reactor (Comelec SA, Figure S15b, Supporting Information) and a preliminary adhesion ALD Al_2O_3 (5 nm) layer was always grown on the substrates whereas a capping parylene C (1 µm) layer completes the sequence to ensure mechanical integrity. The cross section of the multilayer encapsulation obtained by Focused Ion Beam (FIB) milling (Figure S15c), highlights the different layers: these barrier encapsulations guarantee conformality, uniformity, and hermeticity. The Mg resistance curves for test cards coated with 1, 3, and 6 dyads, exposed to wet air (85 °C, 85%RH) are collected in Figure 3c, with the corresponding WVTR curves in Figure 3d. The WVTR initially increases, correspondingly to the transient time for water diffusion in the barrier: in this regime Mg progressively corrodes and the WVTR value corresponds to the real performance of the barrier. Then, it reaches a peak corresponding to the maximum permeation rate of water molecules. Finally, the massive appearance of the hydroxide leads to a decrease in the WVTR until the electrical connection is lost. As illustrated in Figure 3e, the critical time for corrosion (i.e., the time needed for completing the Mg corrosion, see the theoretical definition in the Supporting Information) is proportional to the number of dyads, whereas the value of the peak WVTR ($WVTR_p$) is exponentially related to that. $WVTR_p$ of $(3.2 \pm 0.8) \times 10^2$, $(1.0 \pm 0.3) \times 10^2$, $(1.1 \pm 0.4) \times 10^1$ g m^{-2} d^{-1} were measured for 1, 3 and 6 dyads, respectively, at 85 °C, 85%RH, whereas the initial values in the transient regime were respectively 1.1×10^1, 2.4×10^{-1}, 3.2×10^{-2} g m^{-2} d^{-1}. The following expression for $WVTR_p$ can be proposed for a parylene-based multilayer encapsulation:

$$WVTR_p = WVTR_{pC} \exp\left(-K_M \cdot N_D\right) \quad (3)$$

where $WVTR_{pC}$ is the WVTR of parylene C (i.e., with 0 dyads); K_M is an experimental constant depending on the material and thickness of the dyads; N_D is the number of dyads. Noteworthy, according to the empirical 10-degree rule (or Baker's rule),[51] 6 dyads would have a WVTR of $\sim 5.0 \times 10^{-4}$ g m^{-2} d^{-1} at 25 °C. The higher barrier performance of the hybrid multilayer encapsulations is due to their specific architecture: water permeation is dominated by defects in the inorganic layers but the presence of the organic interlayers decouple the defects, making the diffusion pathway of water molecules more tortuous, resulting in a lower transmission rate.[5,7] To support this concept, a detailed MATLAB-based Finite Element Model (FEM), reported in the Supporting Information, provides insights on the Fickian water diffusion through multilayer barriers (Figure S16, Supporting Information), accounting for the number of defects in each inorganic layer (Figure S17, Supporting Information), the number of inorganic layers and the widths of the defects (Figure S18, Supporting Information), the randomized location of defects and side effects (Figure S19, Supporting Information). It can be shown that the WVTR curve is strongly related to the water concentration versus time profile (Figure S20, Supporting Information): see the theoretical foundation in the Theory section of the Supporting Information.

The critical time for corrosion (t_c) was instead determined by considering a threshold for the electrical resistance (10kΩ) above which the corrosion is assumed complete. We found 16.5, 37, and 75 days at 85 °C and 85%RH for 1, 3, and 6 dyads, respectively. These values match what was reported previously,[7] revealing a linear relationship with the number of dyads (i.e., $t_c = t_c^{pC} + K'_M \cdot N_D$, where t_c^{pC} is the critical time of corrosion with parylene C and K'_M is another experimental constant depending on the nature of the dyads). What is reported in this section demonstrates the versatility and universality of the e-Mg test.

2.1.3. Reproducibility, Lower-Detection Limit, and Comparison with Standard WVTR Measurements

We next evaluated in detail the accuracy of the proposed method (Mg test), in particular its reproducibility and the lower-detection limit (sensitivity).

The reproducibility was investigated by characterizing four test cards coated with parylene C (5 µm), in the same testing conditions, i.e., 85 °C, 85% RH, and soaking in PBS at 85 °C. The Mg corrosion in liquid occurs faster than in wet air, and in both cases, the four measurements follow the same trend, as shown by the resistance curves (Figure 3f). The WVTR for parylene C, and for any encapsulation presented in this work, was determined as the integral mean in the initial regime of the measurement, taking into account the amount of time necessary for water molecules to pass through the barrier and initiate the corrosion process. In order to account for the realistic diffusion process taking place in the barrier/$Mg(OH)_2$ bilayer, a range of $10^{-11} - 10^{-10}$cm^2 s^{-1} can be considered for the diffusion coefficient of parylene[52] at 25 °C (thus $10^{-10} - 10^{-9}$ cm^2 s^{-1} at 85 °C). Hence, Fick's second law yields $t \approx 20 - 200$ s for 5 µm-thick parylene C, therefore the first ≈3 min measurements were selected for the integral mean (see Figure S14b, Supporting Information). The result for one dataset (one Mg stripe) was $\approx 2.2 \times 10^2$ and $\approx 2.0 \times 10^2$ g m^{-2} d^{-1} for PBS, 85 °C, and water vapor 85 °C, 85%RH (in accordance with values found in literature[5,49]), with a root-mean-square deviation of $\approx 0.5 \times 10^1$ g m^{-2} d^{-1} (excluding 10% outliers).

Considering soaking tests in PBS, averaging over four samples yielded $(2.2 \pm 0.3) \times 10^2$ g m^{-2} d^{-1} with a coefficient of variation of 0.15. Within this good reproducibility, deviations in the experiments can be ascribed to the substrate cleaning process, the quality of Mg deposition, non-uniformities in the Mg thickness, and inhomogeneities (e.g., pinholes) of the barrier.[30]

The accuracy of the e-Mg test was investigated by determining the sensitivity of the electronic interface used for real-time monitoring of electrical resistance. In particular, connecting to the multiplexing acquisition board four fixed resistors (4.7, 47, 199, 989 Ω) in place of the e-Mg test cards (see the Supporting Information for details), the variations in the measured resistance were only due to signal fluctuations and instrumental noise (Figure S21a, Supporting Information). The change in resistance is the same for the four resistors, but the change in conductance and thus the apparent WVTR ($WVTR_{app}$) depends on the value of the resistor (Figure S21b–d, Supporting Information): the higher the resistance, the lower the $WVTR_{app}$. A value of 1×10^{-9} g m^{-2} d^{-1} was obtained for the highest resistance used, thus representing the electronics sensitivity limit. The lower experimental detection limit was instead measured using rigid e-Mg test cards enclosed with a glass slide edge-sealed (with several applications of PIB and epoxy) and soaked in PBS at 85 °C (Figure S21e, Supporting Information), similarly to what was reported for previous works on Ca test.[30,53] This sample, in fact, represents the closest case to an ideal encapsulation: the only sources of Mg corrosion were the slight water permeation through the sealed interface, the reaction with the glass, the outgassing from the sealant and the residual O_2/H_2O remained entrapped between Mg and glass during the assembly (performed in a glove box). The presence of N_2 between Mg and glass, as well as the irregular sealed interface contributed to delay the Mg degradation. Therefore, in these conditions, the Mg corrosion rate can be reasonably considered as the minimum detectable rate. Figure 3g shows the resistance increase for three Mg test lines (3.1, 5.2, 7.5 Ω), whereas Figure 3h reports the corresponding WVTR curves: a value of 2.1×10^{-5} g m^{-2} d^{-1} was obtained for the 7.5 Ω Mg test line, which corresponds to a value of 3.3×10^{-8} g m^{-2} d^{-1} for a pattern of ≈10^2 Ω (as in real case for micro-patterns in bioelectronic implants) at 25 °C. This sensitivity is unprecedently lower than that of the electrical Ca test (≈1×10^{-7} g m^{-2} d^{-1} at 25 °C[30]) which has been considered so far, together with the radioactive tritium test,[54] the most accurate method for detecting water permeability.

Therefore, compared to standard bulky systems (e.g., Mocon apparatus, 5×10^{-5} g m^{-2} d^{-1} sensitivity;[55] Technolox mass spectrometer, 1×10^{-5} g m^{-2} d^{-1} sensitivity;[56] Systech Instrument 7001, 2×10^{-3} g m^{-2} d^{-1} sensitivity (Figure S21, Supporting Information), etc.) the e-Mg test presents: i) higher sensitivity; ii) compatibility with microfabrication technology; iii) suitability for miniaturization; and iv) versatility of testing conditions including broader operational temperature range.

For instance, a representative standard water permeation cell for WVTR measurements (Systech Instrument 7001, requires the barriers to be free-standing or on a carrier substrate, (see measurements for several standard encapsulations in Figures S23–S26, Supporting Information). The system cannot be used to evaluate performances of ultrahigh-barrier encapsulations, e.g., a PI carrier substrate coated with a 3-dyad hybrid encapsulation (Figure S27, Supporting Information) provides values very close to the low detection limit of the system, with wide fluctuations and negative WVTR values, thus not reliable. More sensitive commercial equipment, based on these standard tests, could be considered (as the aforementioned Mocon[55]) but nonetheless, any measurement close to the lower detection limit that may cause saturation/drying issues of the permeation cells should not be taken as reliable. This further demonstrates the utility of the proposed method, which is anyway in good agreement with the values provided by the standard system within their own operating conditions (Table S2, Supporting Information).

2.2. Flexible and Stretchable e-Mg Test Cards

2.2.1. Flexible e-Mg Test Cards

Next, we fabricated flexible versions of the rigid e-Mg test cards, hereafter called flexible e-Mg test cards (see the full fabrication process in Figure S28, Supporting Information). **Figure 4a** shows two representative Mg designs (narrower (150 µm) and wider (500 µm) serpentines) embedded between two 5 µm-thick layers of PI. The deposited Mg films (200 nm) were high-quality, crack-free, highly reflective, and not affected by the subsequent baking and curing of the PI superstrate. The flexible test cards enable to perform a dynamic e-Mg test, i.e., introducing mechanical deformations during the Mg corrosion. Soft bioelectronic implants, in fact, must be shape-adaptable and undergo movements/deformations due to the body motions or the contraction/expansion of internal organs. To evaluate the mechanical integrity and compliance of the test cards in operational conditions, we performed cyclic buckling tests (Figure 4a) on a horizontal cyclic stretcher (Figure S29a, Supporting Information). The cyclic limits were set in accordance with physiological conditions,[57] i.e., relative axial displacements (40% and 60%) and two motion frequencies (0.1 and 1 Hz; Figure S29b, Supporting Information). We determined the applied strain (ϵ_x) and stress (σ_x^{Mg}) in the Mg thin films (Figure S29b, Supporting Information), from the theory of solid mechanics ($\epsilon_x = y/R$, $\sigma_x = E\epsilon_x/(1-\nu^2)$, where y is the distance from the neutral axis, R is the radius of curvature, E, ν the Young's modulus and Poisson's ratio of the material under stress). We found 2.44 and 4.03 MPa (σ_x^{Mg}) for 40% and 60% relative displacements, respectively. The corresponding strains were 4.9 and 8.1×10^{-5}, thus not risky for any mechanical damage. Correspondingly, the electrical resistance of the flexible test cards did not exhibit any change during the buckling tests after 140 000 cycles (Figure 4b). When performing mechanical tensile tests up to break, the resistance increased smoothly until the abrupt increase (with elongation at break of ≈3–4%) (Figure S29c, Supporting Information). This confirms the good quality and mechanical integrity of the deposited Mg films. We characterized then the test cards in PBS at 25° in static and dynamic mode. After soaking (Figure S29d, Supporting Information), the Mg converts into hydroxide and becomes transparent. Figure S29e,f (Supporting Information) shows an FIB-milled cross section of a flexible test card where the Mg profile can be observed. EDX analysis revealed that the oxidation took place with the appearance of O in place of Mg (Figure S29f, Supporting Information). In Figure S29g (Supporting Information), a magnified SEM

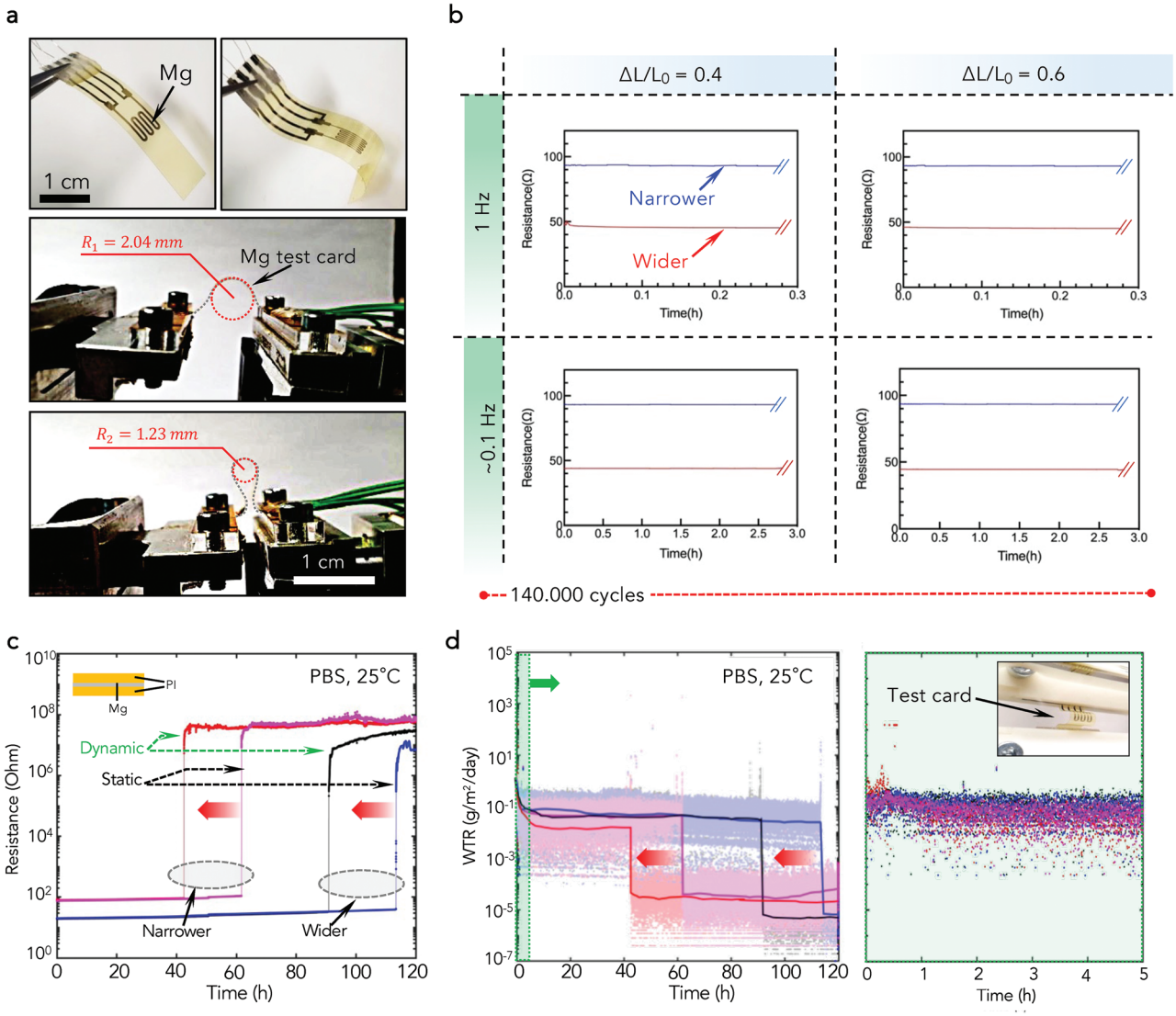

Figure 4. Dynamic testing of flexible Mg-test cards. a) Photos of the flexible e-Mg test cards (two representative designs) and buckling tests with two fixed relative displacements (the corresponding radii of curvature are shown). b) Results of resistance monitoring during the buckling tests at two different frequencies and two fixed displacements. c) Resistance-time curves for soaking tests of flexible e-Mg test cards in PBS at 25 °C, in static and dynamic mode. The corresponding WTR curves are reported in (d). The inset shows the flexible test card in a buckled shape during soaking.

image shows the porosity of the hydroxide embedded in PI. The asymmetric structure resulting after the corrosion is due to the presence of the Ti seed layer which acts as a barrier from one side of Mg. For the dynamic mode, we used a chamber filled with PBS (Figure S29g, Supporting Information) in which the test cards were subjected to buckling tests (Figure S29h, Supporting Information). From the resistance and WTR curves (Figure 4c,d) we deduced that the dynamic mode does not affect the water transmission rate but only the critical time for completing the corrosion, in fact the resistance curves appeared shifted leftwards compared to those in static mode. The effect of the mechanical buckling onto the corrosion can be ascribed to an accumulated damage that enhances corrosion, but the water diffusivity through the barrier does not change: in fact, the tested deformations were not large enough to enhance cracking and favor the water permeation and corrosion. In particular, an initial WTR of $\approx 2.0 \times 10^{0}$ g m^{-2} d^{-1} was obtained for all the designs and modes in PBS at 25 °C (Figure 4d), which corresponds to a value of $\approx 1.3 \times 10^{2}$ g m^{-2} d^{-1} at 85 °C. The inset in Figure 4d shows the curves initially stable and with a slight negative slope which leads, after ≈10 h, to a plateau at $\sim 5 - 9 \times 10^{-1}$ g m^{-2} d^{-1} (averaged), corresponding to the hydroxide contribution. Since the WTR does not change, a control test with rigid test cards coated with PI is not needed. A further benefit of the flexible e-Mg test cards is that they can detect mechanical failure, since this would lead to distinguishable signatures in the electrical measurements. Since cracking is an immediate phenomenon, this would lead to abrupt and stepwise increases in the Mg resistance, whereas the increase induced by corrosion is more asymptotic until the loss of connection.

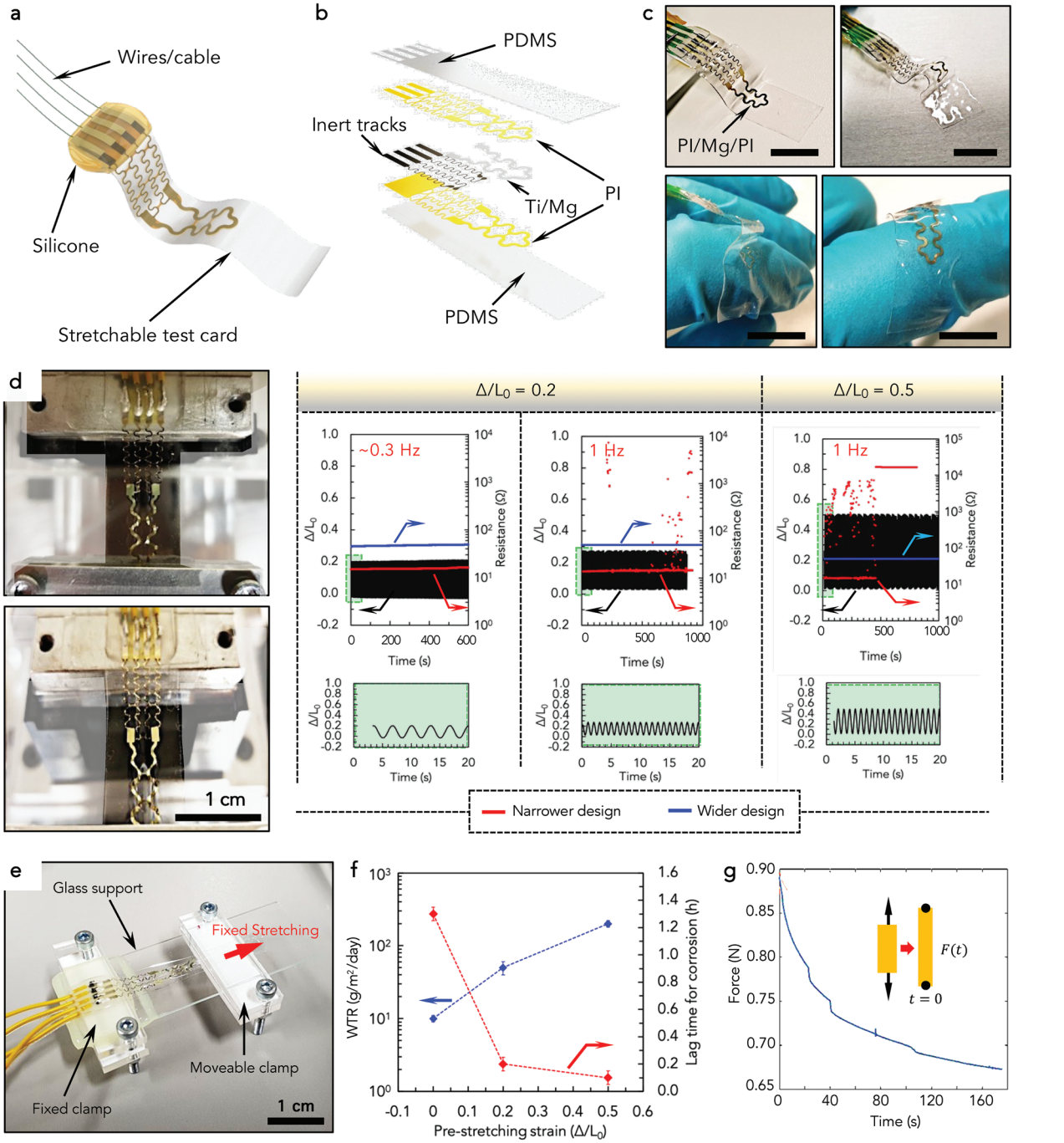

Figure 5. Stretchable e-Mg test cards. a,b) Illustration (a) and exploded view (b) of the stretchable e-Mg test cards. c) Real photos of stretchable test cards with two different representative designs for Mg (narrower and wider). d) Tensile cyclic tests for stretchable test cards with narrower and wider Mg pattern, at two displacements (Δ, L_0 are the elongation and the initial length) and for two representative stretching frequencies. The black curves are the displacement-time curves. e) Corrosion tests during the application of a fixed stretching strain, using two clamps. f) WVTR values and lag time for corrosion, for the same stretchable test card subject to three different pre-stretching strains and soaked in PBS at 85 °C. g) Stress relaxation curve for a stretchable test card subject to an initial pre-stretching strain of 50%.

2.2.2. Stretchable e-Mg Test Cards

Next, we designed proof-of-concept stretchable e-Mg test cards (**Figure** 5a–c), by introducing serpentines, patterned in the PI/Mg/PI stack (see the full fabrication process in Figure S30, Supporting Information). We first evaluated the mechanical response of the stretchable test cards by performing uniaxial tensile tests and monitoring their electrical resistance. FEM simulations of the soft structures under an applied 100% elongation indicate maximum von Mises stresses of 5.0 MPa and ≈400 MPa

in the PDMS and in the PI/metal/PI serpentines, respectively (Figure S31a,b). Lowering the width and the stiffness of the Mg pattern generally allows a more homogeneous elongation and reduces the maximal stresses. Further design optimization could be performed to achieve desired levels of stretchability, but this is not within the scope of this work. Figure S31c,d (Supporting Information) shows the force-displacement curves and the electrical resistance monitoring for the quasi-static up-to-break tensile tests: on average, the narrower design reached a strain of 80% without losing electrical contact and keeping a stable resistance up to 40% strain, exhibiting thus a better stretchability. The next increase in resistance upon elongation is attributed to the creation of lattice defects and cracking in the Mg thin films. We also carried out dynamic cyclic stretching tests in ambient conditions to evaluate the long-term mechanical response: we clamped the devices on a cyclic stretcher and performed cycles with two representative frequencies (0.3 and 1 Hz) and two relative axial displacements (20% and 50%). As shown by the displacement-time curves and the resistance monitoring (Figure 5d), the wider design exhibited a more stable signal whereas the narrower one had degraded performances with increasing displacement and frequency. At 1 Hz and 50% displacement, the stability reached 500 cycles for the narrower design.

Next, we analyzed the corrosion rate of the stretchable e-Mg test cards with static soaking tests in PBS at 85 °C, without or with pre-stretch. Figure S31e (Supporting Information) shows the resulting test cards after Mg corrosion, and Figure S31f (Supporting Information) reports the corresponding resistance curves and WTR plots: a WTR of 1.8×10^1 g m^{-2} d^{-1} was obtained for the PDMS/PI encapsulation at 85 °C, which is in line with the results achieved with the flexible test cards, confirming the very high permeability of PDMS.[5] Based on the transmission rate values of PDMS found with standard measurements (Figure S24, Supporting Information), normalized to its thickness in the stretchable test cards and to the testing temperature, a WTR of $\approx 1.47 \times 10^2$ g m^{-2} d^{-1} can be extracted for PI. This value compares well with the value of 1.3×10^2 g m^{-2} d^{-1} obtained for the flexible e-Mg test cards.

Next, we pre-stretched the test cards by clamping them on a glass support at a specific displacement (Figure 5e), and then soaked them in PBS at 85 °C. The Mg corrosion exhibited a strong acceleration upon strain and the WTR of the encapsulation increased by a factor of 4.3 when stretched to 20% strain (Figure 5f). In particular, we obtained 1.1×10^1, 4.7×10^1, 1.6×10^2 g m^{-2} d^{-1}, for 0%, 20%, and 50% pre-strain, respectively. Since the previous tests demonstrated a good Mg mechanical integrity at these strains, the effect of stretching-enhanced water permeation may be attributed to a larger free-void volume in the polymeric barriers,[58–60] to possible micro-delamination between PDMS and PI, or to the temporarily reduced thickness of the encapsulation during to the deformation, which allows water to penetrate through the encapsulation more rapidly. Additionally, the stress relaxation in the polymers (Figure 5g), the redistribution of stresses, and the plastic deformation around Mg (which occurs rapidly) can play a role in accelerating the water diffusion and the Mg corrosion.[61,62]

Finally, given the softness and shape-adaptability of the stretchable test cards, we tested them in a real biological tissue. We implanted them into beef sirloins as tissue phantoms, kept at body temperature (37 °C) for >5 h (the detailed procedure is described in the Supporting Information). The resulting WTR (9.2×10^0 g m^{-2} d^{-1}, (Figure S31g,h, Supporting Information) was of a similar order of magnitude to the ones measured at 85 °C in PBS, revealing that the biological tissue constitutes a more aggressive physiological environment than a buffer solution and can accelerate any degradation/permeation pathways in plastics.[63–68] Further tests with wider variability of tissues and with deep histological/biochemical analyses would be needed to understand whether the permeability of the polymer encapsulation to water molecules could vary in relation to the molecules present in these bio-environments. However, this preliminary result confirms that exposure to biological tissue does play an important role in water permeation through the encapsulation.

2.3. Implementation of e-Mg Test within Neural Interfaces

Next, we integrated the e-Mg test into two representative microfabricated neural interfaces, i.e., flexible electrocorticography (ECoG) electrode arrays and stretchable optoelectronic implants (optoelectrodes). Neural interfaces are, in fact, an exemplary category of bioelectronic devices, mostly implanted, interacting with the nervous system and requiring optimal reliability.

ECoG implants were manufactured according to an established process flow (Figures S32 and S33, Supporting Information): a resistive Mg sensor and inert metallic (Ti/Pt) interconnects were embedded in 5µm-thick PI exposing electrodes through the top PI (Figure S33c, Supporting Information); the Mg sensor was patterned as a four-point-probe (4PP)-connected Mg ring around the inert electrode (Figure S33d, Supporting Information), leaving a gap of 10 µm to avoid undesired delamination at the PI/electrode interface due to the swelling of the corroding Mg and without hindering the water permeation through the PI encapsulation.

We soaked a 3-electrode ECoG in PBS at 85 °C and monitored the resistance between two adjacent electrodes isolated from the solution with PIB: water permeation induced a 10^2-fold decrease in the inter-electrode resistance (from 10^6 to $10^4\Omega$) (Figure S33f, Supporting Information) within a day of exposure to PBS. Water diffusion likely occurred through the encapsulation's surface and/or through its sidewalls (Figure S33h, Supporting Information). The time at which the resistance decrease occurs was even shorter than the theoretical time necessary for water diffusion between electrodes (according to the approximation $\Delta t \approx d_{IE}^2/6D$, where d_{IE} is the inter-electrode distance): this could be ascribed to other effects such as water permeation at the interfaces.

Integrating the Mg sensor into the ECoG offers real-time quality control for the encapsulation and device performance. Mg oxidation does not affect the integrity of the interfaces in the implant (Figure S33g, Supporting Information), maintaining a good PI/electrode adhesion. We tested the devices ex vivo on the surface of pigs' explanted brains (Figure S34a, Supporting Information), keeping the implants always in contact with the tissue surface, at body temperature (≈37 °C), and hydrated in a PBS bath. The e-Mg resistance curves for the corroding Mg rings (**Figure 6a**) show that the critical time for completing corrosion matches the time spent before the cross-talk occurred between the electrodes, meaning that Mg can detect the inter-electrode

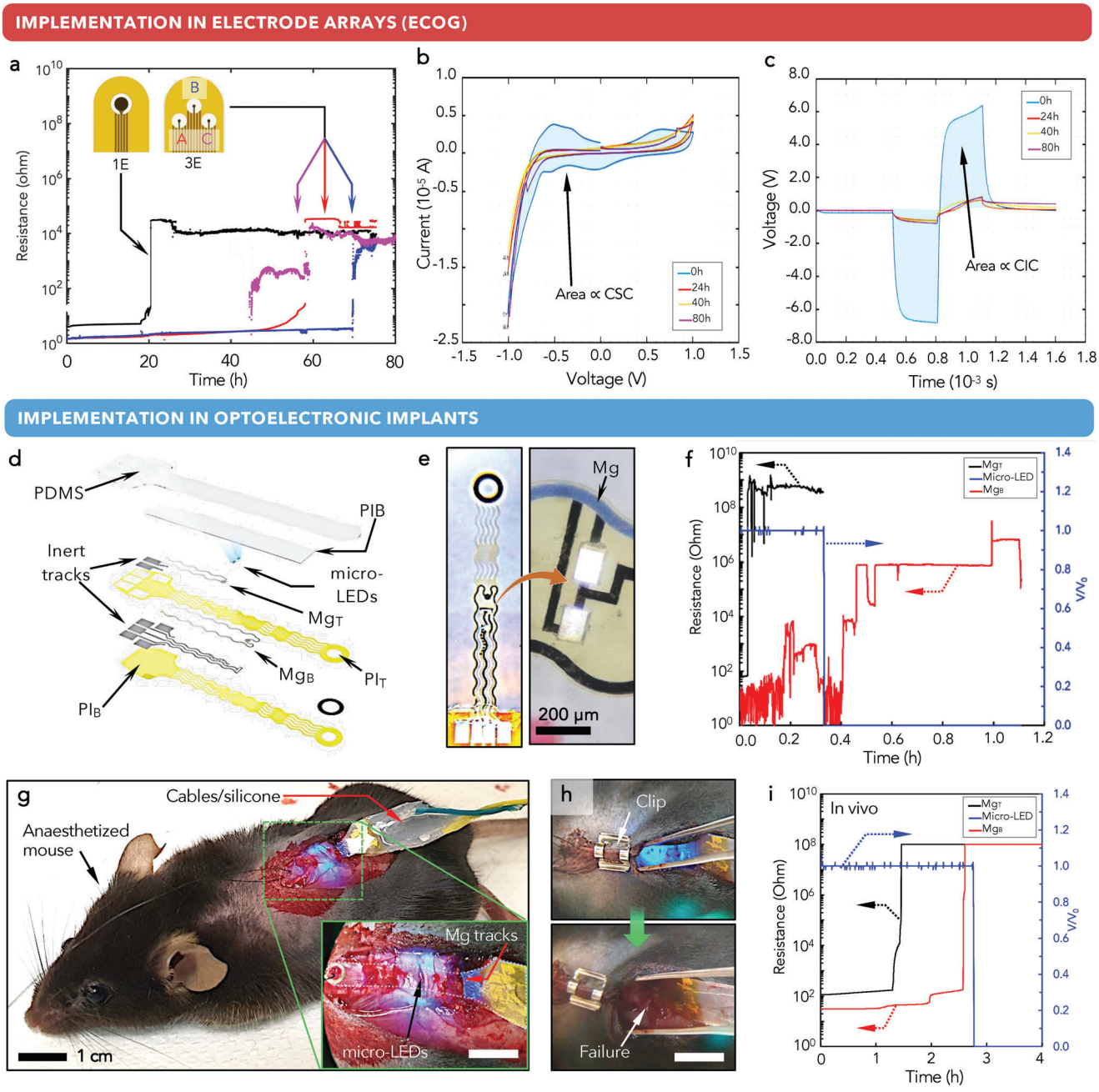

Figure 6. Implementation of e-Mg test in neural interfaces. a) Resistance curves for the Mg patterns in the 1-electrode and 3-electrode ECoG designs for ex vivo measurements. b,c) Chronic electrical characterization of the ECoG implants ex vivo: b) CV, c) VT curves. CSC, charge storage capacity; CIC, charge injection capacity. d) Exploded view of the stretchable optoelectrode with bottom and top Mg tracks for measuring permeability. e) Optical micrograph of the implant with a focus on the micro-LEDs integrated in the design. f) In vitro monitoring of the micro-LED operation and of the bottom and top Mg tracks (Mg_B and Mg_T, respectively), soaked in PBS at 85 °C. g) In vivo implantation of the Mg-integrated devices in the spinal cord of anesthetized mice. The inset shows the micro-LED function inside the epidural space. h) Zoom on the implantation site and on the micro-LED operation, before and after its failure. i) In vivo monitoring of the micro-LED operation and of the bottom and top Mg tracks.

leakages. The results of the e-Mg test can then be correlated with the electrical performances of the devices. As shown by the electrochemical impedance spectroscopy (EIS), cyclic voltammetry (CV), and voltage-transient (VT) curves of the implants applied on the tissue (Figure S34b, Supporting Information, and Figure 6b,c), at the same time when the crosstalk occurs, several changes appear: an increase in the EIS impedance, a 40% reduction in the area enclosed by the CV curves, and a flattening of the VT curves. These effects can be ascribed to the degradation of the electrodes/tissue interface, and the resulting charge storage/injection capacity of the ECoG.[27] In summary, the e-Mg test provided the time at which a 40% loss in performance occurred

for the ECoG implant during its deployment, besides being a useful tool to monitor real-time the WTR of the encapsulations in contact with the host tissue.

In a follow-up experiment, we demonstrated the miniaturization and integration of the e-Mg test into stretchable optoelectrodes aimed for applications in optogenetics across the dorsoventral spinal cord of mice. The implants carry micro-LEDs (dimensions 270×220×50 μm^3, wavelength 470 nm) to deliver blue light across the spinal cord (Figure S35, Supporting Information[69]). We integrated two stretchable Mg tracks into the optoelectrodes, one per encapsulation film: the first PI encapsulation embeds the metal interconnections, whereas on top of it the micro-LEDs are soldered and encapsulated with elastomers (e.g., PDMS and/or PIB) (Figure 6d). Therefore, the two stretchable Mg tracks (bottom, Mg_B and top, Mg_T) were deposited and patterned below the PI and the PDMS encapsulants, respectively (Figure S36, Supporting Information). Through in vitro accelerated aging tests in PBS at 85 °C, we obtained the resistance curves for the two Mg tracks as well as the normalized voltage on the micro-LEDs (Figure 6f). The optical devices worked properly with stable voltage until sudden electrical failure. The top Mg track corroded faster than the bottom one, failing in few minutes, in line with PDMS high permeability. Interestingly, the micro-LEDs remained functional after the failure of the first encapsulation and stopped working before the failure of the second encapsulation. This can be ascribed to the weakening of the soldering sites due to water permeation. So far, the micro-LED's lifetime was taken as a metric for the barrier lifetime;[7] here we demonstrate that the failure processes occurring during the implant operation are more complex and the e-Mg test unprecedently provides a more accurate method to search for the cause of the barrier/device failure. Additionally, it allows for a real-time and dynamic monitoring during implantation against the qualitative "on/off" indication given by the micro-LED's lighting.

We implanted the optoelectrodes into the spinal cord of terminally anesthetized mice in an acute setting (Supporting Information Notes and Figures S37 and S38a–e, Supporting Information; Figure 6g). After closing the wound with skin clips, the light of the micro-LEDs was observable (Figure S38f, Supporting Information), and tunable by adjusting their modulation current (Figure S38h, Supporting Information). The performance of the micro-LEDs was monitored over time (Figure 6h and Figure S38g, Supporting Information) together with the Mg electrical resistance. The corrosion of the Mg tracks was completed in a few hours (faster for Mg_T, Figure 6i) and correspondingly the micro-LEDs stopped working in between, matching our in vitro observations. WTR values of $\approx 5.6 \times 10^{-1}$ and 3.3×10^{0} g m^{-2} d^{-1} were respectively extracted for PDMS/PI (Mg_B) and PDMS (Mg_T), which follow the trend found previously with flexible and stretchable test cards (in vitro/ex vivo).

3. Conclusions

In summary, we developed an e-Mg test as a universal and ultrasensitive method for measuring the permeability of any barrier encapsulation used in bioelectronic implantable applications. The method is based on the use of resistive sensors and on the correlation between the Mg corrosion rate with the water transmission rate of the barrier. The miniaturized transducer can be integrated into neural implants, providing in situ and real-time quality control for the encapsulation and the device itself. Mg films can be patterned to be included in the design of miniaturized implants. We demonstrated their integration and use in two typical neural interfaces, an ECoG and a spinal cord epidural implant. The Mg sensor method exhibits good accuracy, reproducibility, and repeatability, matching values provided by standard WTR measuring systems. The thin-film sensor approach is versatile and reliable, provides quantitative feedback on the exposed devices, and allows to achieve ultra-low detection limit of water permeation (3×10^{-8} g m^{-2} d^{-1}) independently on the use conditions, from in vitro to in vivo settings. This is also a useful technique to assess in situ performance of thin film encapsulation, which remains an unmet challenge for long-term bioelectronic implants. The Mg test can also reveal critical phenomena such as encapsulation failure or electrical degradation of electrodes. In conclusion, the development of this miniaturized, quantitative approach to device aging is poised to significantly enhance the application scope and efficacy of wearable and implantable bioelectronics, offering new avenues for advancement in this field.

4. Experimental Section

Detailed fabrication steps for the devices, designs for the data acquisition systems, and related hardware, the in vitro and ex vivo/in vivo setups are described in Supporting Information.

Supporting Information

Supporting Information is available from the Wiley Online Library or from the author.

Acknowledgements

The authors would like to acknowledge financial support by InnoSuisse grants 45944.1 IP1643 ENG "FLEXCAN: Flexible Encapsulation of active implants". The authors would like to thank the staff at the Neural Microsystems Platform of of Fondation Campus Biotech Geneva for their help with the fabrication processes, all the staff at EPFL Cmi and the staff at EPFL CIME for assistance in samples' preparation.

Open access funding provided by Ecole Polytechnique Federale de Lausanne.

Conflict of Interest

The authors declare no conflict of interest.

Author Contributions

Y.L. and S.P.L. contributed equally to this work. M.M. conceived the experiments, designed and fabricated all the test cards and implants described in the work, performed the aging and corrosion tests and the FEM modelling; S.P.L., Y.L., and M.V.G. acquired funding and managed the project; K.A. carried out all the FEM simulations on water permeation through multilayer encapsulations; C.B. fabricated and characterized thoroughly the Mg-integrated ECoG devices; K.W. provided support for the fabrication and characterization of flexible e-Mg test cards and the Mg-integrated ECoG

devices; L.W. contributed to the fabrication and characterization of the flexible test cards; M.B.C. contributed to the characterization of the rigid test cards; L.M. contributed to the fabrication and characterization of the stretchable test cards and the FEM mechanical analysis; L.A.J. monitored Mg thin films with different initial thickness; I.F. designed the electrical PCBs used for the e-Mg test multiplexed measurements; C.K. performed the surgeries for implantation of the Mg-integrated optoelectrical devices into mice's spinal cord. G.C. provided laboratory space for animal experimentation. M.V.A. performed the depositions of hybrid multilayer encapsulations; S.P.L. and Y.L. supervised the project and the experiments. M.M. wrote the original draft of the manuscript and made the 3D illustrations and graphics; M.M., S.P.L., and Y.L. reviewed and edited the manuscript.

Data Availability Statement

The data that support the findings of this study are available from the corresponding author upon reasonable request.

Keywords

barrier encapsulations, bioelectronic implants, ECoG, ex vivo, in vitro, in vivo, magnesium, neural interfaces, optoelectrodes, permeability-measuring methods, water transmission rate

Received: December 4, 2023
Revised: March 5, 2024
Published online: April 30, 2024

[1] A. Burton, S. M. Won, A. K. Sohrabi, T. Stuart, A. Amirhossein, J. U. Kim, Y. Park, A. Gabros, J. A. Rogers, F. Vitale, A. G. Richardson, P. Gutruf, *Microsyst. Nanoeng.* **2021**, *7*, 1.
[2] M. Palma, M. Khoshnevis, M. Lion, C. Zenga, S. Kefs, F. Fallegger, G. Schiavone, I. G. Flandin, S. Lacour, B. Yvert, *J. Neurosci. Methods* **2022**, *366*, 109427.
[3] M. Capogrosso, T. Milekovic, D. Borton, F. Wagner, E. M. Moraud, J.-B. Mignardot, N. Buse, J. Gandar, Q. Barraud, D. Xing, E. Rey, S. Duis, Y. Jianzhong, W. K. D. Ko, Q. Li, P. Detemple, T. Denison, S. Micera, E. Bezard, J. Bloch, G. Courtine, *Nature* **2016**, *539*, 284.
[4] M. Zamora, R. Toth, F. Morgante, J. Ottaway, T. Gillbe, S. Martin, G. Lamb, T. Noone, M. Benjaber, Z. Nairac, D. Sehgal, T. G. Constandinou, J. Herron, T. Z. Aziz, I. Gillbe, A. L. Green, E. A. C. Pereira, T. Denison, *Exp Neurol* **2022**, *351*, 113977.
[5] M. Mariello, K. Kim, K. Wu, S. P. Lacour, Y. Leterrier, *Adv. Mater.* **2022**, *n/a*, 2201129.
[6] M. Mariello, K. Wu, M. von Allmen, M. van Gompel, S. P. Lacour, Y. Leterrier, presented at Proc. of the 2022 IEEE Int. Conf. on Flexible and Printable Sensors and Systems (FLEPS), Vienna, Austria, July **2022**.
[7] K. Kim, M. Van Gompel, K. Wu, G. Schiavone, J. Carron, F. Bourgeois, S. P. Lacour, Y. Leterrier, *Small* **2021**, *17*, 2103039.
[8] S. P. Lacour, G. Courtine, J. Guck, *Nat. Rev. Mater.* **2016**, *1*, 1.
[9] I. R. Minev, P. Musienko, A. Hirsch, Q. Barraud, N. Wenger, E. M. Moraud, J. Gandar, M. Capogrosso, T. Milekovic, L. Asboth, R. F. Torres, N. Vachicouras, Q. Liu, N. Pavlova, S. Duis, A. Larmagnac, J. Vörös, S. Micera, Z. Suo, G. Courtine, S. P. Lacour, *Science* **2015**, *347*, 159.
[10] K. C. Cheung, P. Renaud, H. Tanila, K. Djupsund, *Biosens. Bioelectron.* **2007**, *22*, 1783.
[11] L.-H. Shi, F. Luo, D. J. Woodward, J.-Y. Chang, *Synapse* **2006**, *59*, 445.
[12] M. Mariello, F. Guido, V. M. Mastronardi, R. Giannuzzi, L. Algieri, A. Qualteri, A. Maffezzoli, M. De Vittorio, *Micromachines* **2019**, *10*.
[13] H. Fang, J. Zhao, K. J. Yu, E. Song, A. B. Farimani, C.-H. Chiang, X. Jin, Y. Xue, D. Xu, W. Du, K. J. Seo, Y. Zhong, Z. Yang, S. M. Won, G. Fang, S. W. Choi, S. Chaudhuri, Y. Huang, M. A. Alam, J. Viventi, N. R. Aluru, J. A. Rogers, *Proc. Natl. Acad. Sci. USA* **2016**, *113*, 11682.
[14] E. Song, H. Fang, X. Jin, J. Zhao, C. Jiang, K. J. Yu, Y. Zhong, D. Xu, J. Li, G. Fang, H. Du, J. Zhang, J. M. Park, Y. Huang, M. A. Alam, Y. Mei, J. A. Rogers, *Adv. Electron. Mater.* **2017**, *3*, 1700077.
[15] S. Minnikanti, G. Diao, J. J. Pancrazio, X. Xie, L. Rieth, F. Solzbacher, N. Peixoto, *Acta Biomater.* **2014**, *10*, 960.
[16] C. Charton, N. Schiller, M. Fahland, A. Holländer, A. Wedel, K. Noller, *Thin Solid Films* **2006**, *502*, 99.
[17] T.-N. Chen, D.-S. Wuu, C.-C. Wu, C.-C. Chiang, Y.-P. Chen, R.-H. Horng, *Plasma Process Polym* **2007**, *4*, 180.
[18] Y. C. Han, E. Kim, W. Kim, H.-G. Im, B.-S. Bae, K. C. Choi, *Org. Electron.* **2013**, *14*, 1435.
[19] M. Vähä-Nissi, P. Sundberg, E. Kauppi, T. Hirvikorpi, J. Sievänen, A. Sood, M. Karppinen, A. Harlin, *Thin Solid Films* **2012**, *520*, 6780.
[20] S.-H. Jen, J. A. Bertrand, S. M. George, *J. Appl. Phys.* **2011**, *109*, 084305.
[21] Y. Leterrier, *Prog. Mater. Sci.* **2003**, *48*, 1.
[22] J. Lewis, *Mater. Today* **2006**, *9*, 38.
[23] Y. Leterrier, in *Handbook of Flexible Organic Electronics* (Ed: S. Logothetidis), Woodhead Publishing, Oxford **2015**, pp. 3–36.
[24] Y. Leterrier, A. Mottet, N. Bouquet, D. Gilliéron, P. Dumont, A. Pinyol, L. Lalande, J. H. Waller, J.-A. E. Månson, *Thin Solid Films 519*, 1729.
[25] F. Fallegger, G. Schiavone, S. Lacour, *Adv. Mater.* **2019**, *32*.
[26] G. Schiavone, F. Fallegger, X. Kang, B. Barra, N. Vachicouras, E. Roussinova, I. Furfaro, S. Jiguet, I. Seáñez, S. Borgognon, A. Rowald, Q. Li, C. Qin, E. Bézard, J. Bloch, G. Courtine, M. Capogrosso, S. P. Lacour, *Adv. Mater.* **2020**, *32*, 1906512.
[27] G. Schiavone, X. Kang, F. Fallegger, J. Gandar, G. Courtine, S. P. Lacour, *Neuron* **2020**, *108*, 238.
[28] M. Mariello, K. Kim, M. Van Gompel, K. Wu, S. P. Lacour, Y. Leterrier, in Proceedings of the International Conference on Micro and Nano-Engineering (MNE), Torino, **2021**.
[29] G. L. Graff, R. E. Williford, P. E. Burrows, *J. Appl. Phys.* **2004**, *96*, 1840.
[30] M. D. Kempe, M. O. Reese, A. A. Dameron, *Rev. Sci. Instrum.* **2013**, *84*, 025109.
[31] G. Nisato, P. C. P. Bouten, P. J. Slikkerveer, W. D. Bennett, G. L. Graff, N. Rutherford, L. Wiese, *SID Conf. Rec. Int. Disp. Res. Conf.* , **2001**, pp. 1435–1438.
[32] G. Nisato, H. Klumbies, J. Fahlteich, L. Müller-Meskamp, P. van de Weijer, P. Bouten, C. Boeffel, D. Leunberger, W. Graehlert, S. Edge, S. Cros, P. Brewer, E. Kucukpinar, J. de Girolamo, P. Srinivasan, *Org. Electron.* **2014**, *15*, 3746.
[33] A. A. Dameron, M. D. Kempe, M. O. Reese, *Rev. Sci. Instrum.* **2014**, *85*, 075102.
[34] L. M. Vrana, in *Kirk-Othmer Encyclopedia of Chemical Technology*, John Wiley & Sons, Ltd, New York **2011**, pp. 1–10.
[35] K. Wu, M. Mariello, Y. Leterrier, S. P. Lacour, *Adv. Mater.* **2024**, *n/a*, 2310201.
[36] R. H. Boyd, P. V. K. Pant, *Macromolecules* **1991**, *24*, 6325.
[37] M. D. Kempe, A. Dameron, T. J. Moricone, M. O. Reese, in 2010 35th IEEE Photovoltaic Specialists Conference, IEEE, Piscataway, NJ **2010**, pp. 000256.
[38] L. Wei, Z. Gao, *RSC Adv.* **2023**, *13*, 8427.
[39] S. Xu, M. Ikpi, J. Dong, J. Wei, W. Ke, N. Chen, *Int. J. Electrochem. Sci.* **2012**, *7*, 4735.
[40] M. A. Aramendıá, J. A. Benıtez, V. Borau, C. Jiménez, J. M. Marinas, J. R. Ruiz, F. Urbano, *J. Solid State Chem.* **1999**, *144*, 25.
[41] J. Wu, J. Du, Y. GAo, *Turk. J. Chem.* **2014**, *38*, 402.
[42] R. N. Abdullaev, R. A. Khairulin, Y. M. Kozlovskii, A. S. Agazhanov, S. V. Stankus, *Trans. Nonferrous Met. Soc. China* **2019**, *29*, 507.
[43] T. Ying, H. Chi, M. Zheng, Z. Li, C. Uher, *Acta Mater.* **2014**, *80*, 288.

[44] C. Vallieres, D. Winkelman, D. Roizard, E. Favre, P. Pscharfer, M. Kind, *J. Membr. Sci.* **2006**, *278*, 357.
[45] H. Klumbies, P. Schmidt, M. Hähnel, A. Singh, U. Schroeder, C. Richter, T. Mikolajick, C. Hoßbach, M. Albert, J. W. Bartha, K. Leo, L. Müller-Meskamp, *Org. Electron.* **2015**, *17*, 138.
[46] R. H. Doremus, *J. Mater. Res.* **1999**, *14*, 3754.
[47] W. F. Gorham, *J. Polym. Sci.* **1966**, *4*, 3027.
[48] M. Mariello, L. Fachechi, F. Guido, M. D. C. Vittorio, *Adv. Funct. Mater.* **2021**, *31*, 2101047.
[49] J. Ortigoza-Diaz, K. Scholten, C. Larson, A. Cobo, T. Hudson, J. Yoo, A. Baldwin, A. Weltman Hirschberg, E. Meng, *Micromachines* **2018**, *9*, 422.
[50] A. Pak, K. Nanbakhsh, O. Hölck, R. Ritasalo, M. Sousa, M. Van Gompel, B. Pahl, J. Wilson, C. Kallmayer, V. Giagka, *Micromachines* **2022**, *13*, 544.
[51] D. W. Waples, *AAPG Bull.* **1980**, *64*, 916.
[52] E. M. Davis, N. M. Benetatos, W. F. Regnault, K. I. Winey, Y. A. Elabd, *Polymer* **2011**, *52*, 5378.
[53] M. O. Reese, A. A. Dameron, M. D. Kempe, *Rev. Sci. Instrum.* **2011**, *82*, 085101.
[54] R. Dunkel, R. Bujas, A. Klein, V. Horndt, *Proc. IEEE* **2005**, *93*, 1478.
[55] AMETEK MOCON OTR & WVTR Permeation Testing for Films & Packages, https://www.ametekmocon.com/products/www.ametekmocon.com/products/permeationanalyzers (accessed: July 2021).
[56] Technolox Permeation Measurement Water Vapour Permeation and Gas Permeation, Instruments and Service Measurements, http://www.technolox.com/ (accessed: October 2023).
[57] H. Chang, J. Chen, Y. Liu, *J Tradit Chin Med* **2018**, *5*, 35.
[58] B. Wernisch, M. A. Otmi, E. Beauvais, J. Sampath, *Mol. Syst. Des. Eng.* **2024**, *9*, 214.
[59] R. Chatterjee, S. Bisoi, A. G. Kumar, V. Padmanabhan, S. Banerjee, *ACS Omega* **2018**, *3*, 13510.
[60] Y. Liu, F. Xie, H. Jie, J. Tan, C. Chen, L. Jiang, W. Sun, H. Zhang, *Polymers* **2021**, *13*, 1749.
[61] R. W. Cox, Ph.D. Thesis, California Institute of Technology, **1988**.
[62] K. Derrien, P. Gilormini, *Defect Diffus. Forum* **2006**, *258–260*, 447.
[63] X.-G. Yang, P.-P. Wen, Y.-F. Yang, P.-P. Jia, W.-G. Li, D.-S. Pei, *Front Microbiol* **2023**, *13*.
[64] N. Mohanan, Z. Montazer, P. K. Sharma, D. B. Levin, *Front Microbiol* **2020**, *11*, 580709.
[65] D. R. Askins, *J. Plast. Film Sheeting* **1985**, *1*, 50.
[66] R. DeIasi, J. Russell, *J. Appl. Polym. Sci.* **1971**, *15*, 2965.
[67] J. A. Cella, *Polym. Degrad. Stab.* **1992**, *36*, 99.
[68] R. Caldwell, M. G. Street, R. Sharma, P. Takmakov, B. Baker, L. Rieth, *Biomaterials* **2020**, *232*, 119731.
[69] C. Kathe, F. Michoud, P. Schönle, A. Rowald, N. Brun, J. Ravier, I. Furfaro, V. Paggi, K. Kim, S. Soloukey, L. Asboth, T. H. Hutson, I. Jelescu, A. Philippides, N. Alwahab, J. Gandar, D. Huber, C. I. De Zeeuw, Q. Barraud, Q. Huang, S. P. Lacour, G. Courtine, *Nat. Biotechnol.* **2021**, 198.